



## ISTITUTO NAZIONALE DI RICERCA METROLOGICA Repository Istituzionale

Textured and Rigid Capillary Materials for Passive Energy-Conversion Devices

*Original*

Textured and Rigid Capillary Materials for Passive Energy-Conversion Devices / Alberghini, M; Morciano, M; Giardino, M; Perrucci, F; Scaltrito, L; Janner, D; Chiavazzo, E; Fasano, M; Asinari, P. - In: ADVANCED MATERIALS INTERFACES. - ISSN 2196-7350. - 9:18(2022), p. 2200057. [10.1002/admi.202200057]

*Availability:*

This version is available at: 11696/75360 since: 2023-02-02T09:55:55Z

*Publisher:*

WILEY

*Published*

DOI:10.1002/admi.202200057

*Terms of use:*

This article is made available under terms and conditions as specified in the corresponding bibliographic description in the repository

*Publisher copyright*

(Article begins on next page)

# Textured and Rigid Capillary Materials for Passive Energy-Conversion Devices

Matteo Alberghini, Matteo Morciano, Matteo Giardino, Francesco Perrucci, Luciano Scaltrito, Davide Janner, Eliodoro Chiavazzo, Matteo Fasano, and Pietro Asinari\*

Passive energy-conversion devices based on water uptake and evaporation offer a robust and cost-effective alternative in a wide variety of applications. This work introduces a new research avenue in the design of passive devices by replacing traditional porous materials with rigid capillary layers engraved with optimized V-shaped grooves. The concept is tested using aluminum sheets, which are machined by femtosecond laser and covered by silica or functionalized by oxygen plasma to achieve stable long-term capillary properties. The durability of the proposed material is experimentally evaluated when functioning with aqueous salt concentrations: both the coated and functionalized specimens exhibit stable wettability after being immersed in saltwater for all the duration of the experiments ( $\approx 250$  h in this work). The proposed new class of materials is envisaged for use in passive solar or thermal energy-conversion devices. As a case study, a time-discretized capillary model is coupled with a validated lumped-parameters heat and mass transfer model, aiming to estimate the maximum size and productivity of a passive solar distiller employing porous materials of known thermal and capillary properties. This study paves the way to the use of a new class of rigid, highly thermally conductive materials that can significantly improve the performance of passive devices by simplifying the assembly of multistage setups, thus helping to extend their use to real-scale applications.

M. Alberghini, M. Morciano, E. Chiavazzo, M. Fasano, P. Asinari  
Department of Energy  
Politecnico di Torino  
Corso Duca degli Abruzzi 24, Torino 10129, Italy  
E-mail: [pietro.asinari@polito.it](mailto:pietro.asinari@polito.it)

M. Alberghini, M. Morciano, M. Giardino, D. Janner, M. Fasano  
Clean Water Center

Corso Duca degli Abruzzi 24, Torino 10129, Italy

M. Giardino, F. Perrucci, L. Scaltrito, D. Janner  
Department of Applied Sciences and Technology  
Politecnico di Torino

Corso Duca degli Abruzzi 24, Torino 10129, Italy

F. Perrucci, L. Scaltrito

Microla Optoelectronics

Per Via Gozzano 34, Chivasso, Torino 10034, Italy

P. Asinari

Istituto Nazionale di Ricerca Metrologica (INRiM)

Strada delle Cacce 91, Torino 10135, Italy



The ORCID identification number(s) for the author(s) of this article can be found under <https://doi.org/10.1002/admi.202200057>.

© 2022 The Authors. Advanced Materials Interfaces published by Wiley-VCH GmbH. This is an open access article under the terms of the Creative Commons Attribution License, which permits use, distribution and reproduction in any medium, provided the original work is properly cited.

DOI: 10.1002/admi.202200057

## 1. Introduction

Capillarity is omnipresent in nature, being directly involved in the functioning of living systems.<sup>[1]</sup> Natural porous media can be characterized by stochastic (e.g., soil, sponges) or ordered (e.g., wood, lungs) structures. Their manmade counterparts are numerous and widely adopted in most industries, for instance filters, textiles (woven and nonwoven), absorbents, ceramics, or tissue scaffolds.<sup>[2]</sup> Engineering the capillary properties of porous materials has been pursued to achieve improved thermal,<sup>[3]</sup> mechanical,<sup>[4]</sup> electrical,<sup>[5]</sup> optical,<sup>[6]</sup> and biomedical<sup>[7]</sup> performance. In addition to intrinsically porous materials (e.g., metal organic frameworks<sup>[8]</sup>), the recent research has focused on manufacturing processes that can control finely either material addition (e.g., 3D printing<sup>[1,9]</sup>) or removal (e.g., laser etching<sup>[6,10]</sup>) from bulk materials to design a precise pores architecture.

Porous materials with engineered multi-functionalities are particularly desirable for passive energy-conversion devices. These devices typically do not require high quality energy inputs and, due to the absence of moving mechanical parts, require low maintenance, and are cost-effective. Moreover, they are optimal for off-grid installations and, in general, promote the sustainable transition of industries related to the water-energy nexus.<sup>[11]</sup> These devices can exploit porous capillary media to overcome small hydraulic heads and supply the working fluids throughout the system without the need for active mechanical or electrical components. Applications have been proposed for steam generation,<sup>[12]</sup> desalination,<sup>[13,14]</sup> salt precipitation,<sup>[15]</sup> water sanitation,<sup>[16]</sup> solar thermal energy harvesting,<sup>[6]</sup> and cooling,<sup>[17]</sup> among others. Clearly, optimizing the capillary properties of the porous materials in such passive devices is crucial to enhance their overall performance: poor capillarity may lead to dry-out during continuous evaporative processes, and would significantly limit the maximum achievable device size.<sup>[18]</sup> Thus, sub-optimal capillary properties would significantly hinder the productivity and scalability of the system overall.

Passive energy-conversion devices typically use nonstructured capillary materials, such as paper or commercial textiles, as passive component to move working fluids.<sup>[19]</sup> These materials, however, offer limited degrees of optimization given

their nonordered structure. Some pioneering works have proved the potential of structured capillary architectures in several areas of heat and mass transfer<sup>[20]</sup> and microfluidics.<sup>[21]</sup> Importantly, we recognize that on one hand the capillary nature of traditional materials is critical for endowing energy-conversion devices with their intrinsic passive nature; on the other hand, the very low thermal conductivity of those materials introduces unavoidable thermal resistances that may detrimentally affect the overall device performance. The availability of metal-based capillary materials with controllable structure may offer new opportunities to effectively attack the above issue, while allowing to design engineered (and stable) pores architectures with microscopic precision and scalability.

This work proposes a different approach to the design of passive components by replacing conventional nonstructured materials with a rigid and micro-structured capillary support. Here, V-shaped grooves were crafted by femtosecond laser etching on high-grade aluminum sheets, however other metals could be used as well.<sup>[22]</sup> In our work, the obtained micro-structure and surface chemistry were analyzed by scanning electron microscope (SEM) imaging and energy dispersive X-ray spectroscopy (EDS) spectroscopy, showing regular and well-defined geometric features. The joint effects of the altered surface chemistry and geometry of the etched cavities provided the treated metal layer with efficient capillary properties. However, prolonged exposure to water depleted the acquired hydrophilicity, coherently with previous evidences widely reported in the literature.<sup>[23–26]</sup> Therefore, both textured and nontextured samples were coated by a nanometers-thick layer of SiO<sub>2</sub> or functionalized by oxygen plasma, and their long-term durability was tested. Notably, the capillary performance of the silica-coated grooved sample remained exceptionally stable for the whole duration of the aging tests in distilled water (≈250 h). Similarly, all the functionalized samples, flat or textured, remained hydrophilic when aged in salt water at 35 g L<sup>-1</sup> (≈230 h of continuous immersion were tested), suggesting the applicability of the proposed concept for, for example, passive thermal desalination. Finally, the capillary properties of the samples were evaluated by vertical wicking tests and compared with those of three other materials used in different passive applications relevant for the water-energy nexus.<sup>[13,17,18,27,28]</sup> The experimental data obtained were used to calibrate a theoretical model relating the average geometry and hydrophilicity of the grooves to their capillary properties, easing the comparison with other structured or nonstructured materials. Moreover, the model was used to predict the geometrical parameters maximizing the capillary properties of the V-shaped channels.

In view of the characterization and analysis performed, the rigid capillary material was envisaged for use in a passive device for solar desalination. A lumped-parameters model for the heat and mass transfer within the device was coupled with the wicking model to investigate the optimal shape of the device in a real-scale application, thus evaluating the actual size and productivity of the engineered assembly. For this purpose, the theoretical model was extended and reformulated in a novel time-discretized scheme consistently including the effect of high evaporation rates. The model was used to extrapolate the performance of a multistage device operating with commercial

hydrophobic membranes, following a traditional device layout. However, the proposed rigid capillary material allows to replace the membranes with air gaps while still avoiding contamination between the saltwater feed and the produced distilled water.

## 2. Results and Discussion

### 2.1. Characterization of the Laser-Etched Material

The rigid novel capillary material was crafted from ultra-pure aluminum plates (Al ≥ 99%), which was selected as reference material given its large abundance, low cost and off-the-shelf availability. The surface of the aluminum sheets was analyzed as-received by SEM imaging and EDS spectroscopy, which revealed minor surface defects and confirmed the high purity of the material with more than 92% Al by weight fraction (wt%) (see Figure S1, Supporting Information). The analysis also revealed negligible traces of oxygen, thus small amounts of oxides were already present on the surface.

Initially inspired by the work of Singh and co-workers,<sup>[6]</sup> a femtosecond laser processing procedure was used to craft homogeneous V-shaped grooves across the entire upper surface of an aluminum plate (see Figure 1A and Experimental Section). This crafting technique was selected due to its high accuracy and flexibility. The etched surface and the geometry of the resulting grooves were inspected by SEM imaging in top-view (see Figure 1B) and section view (see Figure 1C). The analysis revealed an exceptional finish and regular geometry of the obtained features: the grooves spacing is regular, while the material in between was not notably affected by the procedure. The analysis revealed an average grooves width of  $w = (13 \pm 3) \mu\text{m}$ , height of  $h_g = (75 \pm 5) \mu\text{m}$  and a tilt angle of  $\alpha = (85.8 \pm 2.6)^\circ$  (see Figure S2, Supporting Information). Moreover, the observation at high magnifications of the processed sample ( $10^8 \times$ ) showed the presence of a nanostructure on the cavity walls (see Figure 1D). This nanostructure is in the form of a fine porosity with dimensions less than a hundred nanometers, which results in an increase in the roughness of the solid-liquid contact area once the grooves are invaded by a fluid.

The chemical composition of the treated surface was analyzed by EDS spectroscopy. The laser-etched grooves presented ≈20–30 wt% of oxygen in the melted zone in proximity of the grooves (see Figure 1E, right panel): the presence of oxides is mainly due to the high-temperature interaction between the treated surface and the surrounding atmosphere. No significant amounts of other elements were detected. Similarly, the lateral areas, slightly altered by the process, showed an increase in oxygen content of 9 wt%, while the untreated zone between the grooves has an oxygen content of only 2 wt% (see Figure 1E, left panel), demonstrating its marginal oxidation and, therefore, the outstanding accuracy of the processing technique used.

The effect of the surface oxidation produced by the laser treatment was assessed by the analysis of the water-aluminum contact angle and vertical wicking tests (see Experimental Section). Despite its high-energy structure, the aluminum samples presented an average contact angle with distilled water of  $\theta_c = (93 \pm 2)^\circ$ , characteristic of a slightly hydrophobic surface, coherently with previous observations on nonpure metal

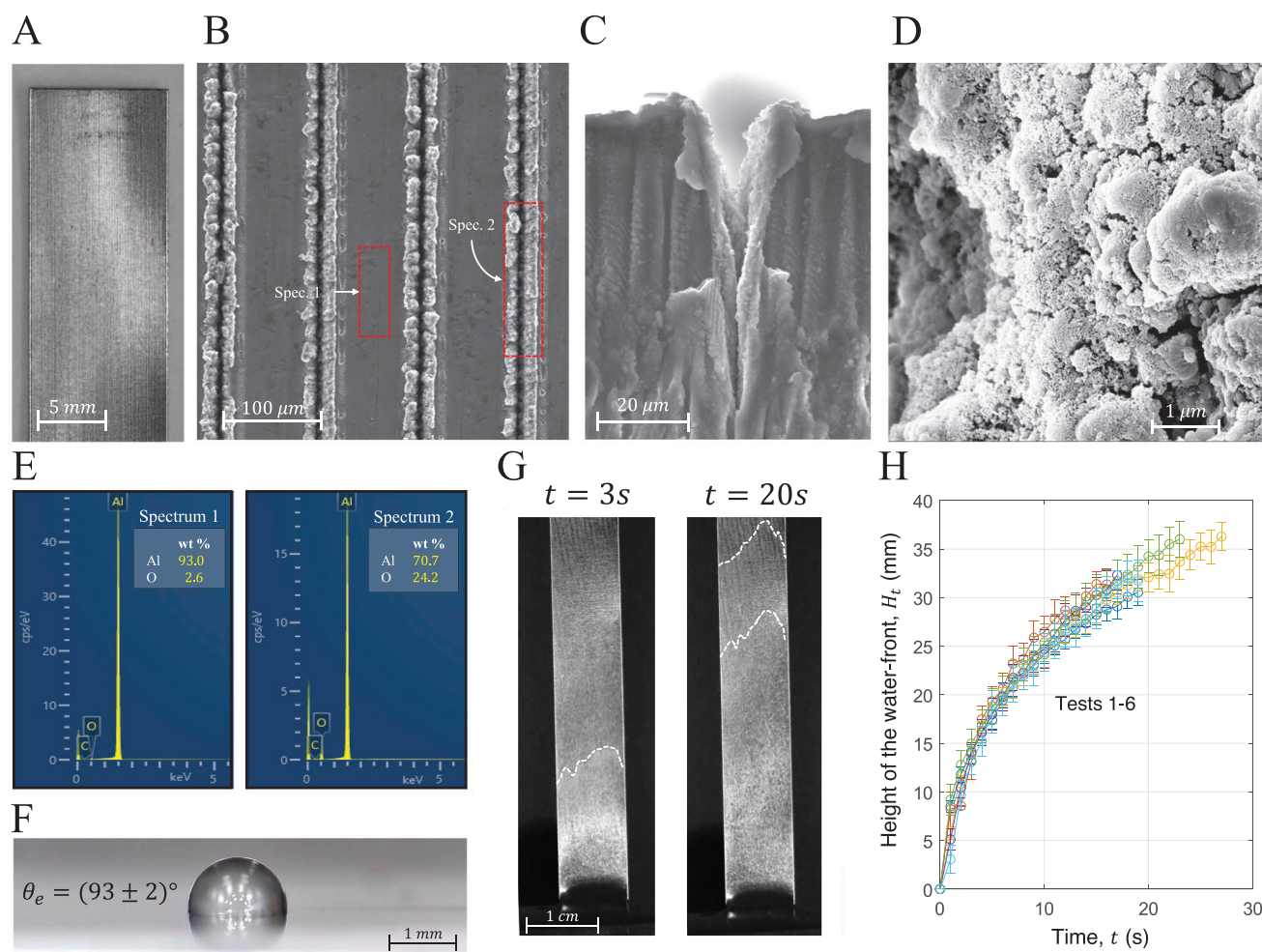


**Figure 1.** Characterization of the laser-etched material. A) A photograph of the crafted material. B,C) SEM images of the laser-etched grooves from the B) top and C) section view, highlighting the realized geometrical features. D) High magnification image of the nanotexture created on the grooves surface. E) EDS spectra of untreated (left) and treated (right) portions of the sample, with reference to panel (B). Elements not shown in the legend were present in a non-significant amount. F) Measurement of the contact angle  $\theta_e$  on the untreated aluminum plate by the static sessile droplet method. G) Progressive images showing the wicking transient in the laser-etched aluminum plate (see also Video S1, Supporting Information). H) The capillary performance of the proposed material was evaluated by means of vertical wicking tests (see Experimental Section). Note that, between each test, the sample was simply dried in open air.

surfaces<sup>[23]</sup> (see Figure 1F). However, the laser-etched specimen was able to promptly wick water as soon as it was dipped into the distilled water reservoir (see Figure 1G and Video S1, Supporting Information). The advancing water front is not flat because the geometry and state of oxidation of the grooves vary slightly from each other: the varying surface roughness, height and angle of inclination determine the different capillary properties of each groove. However, the short-tails of their distribution allow to identify the moving water front in a range of few millimeters. The acquired images were translated into quantitative data by an image-processing tool (see Experimental Section) and were used to evaluate the wicking performance of the crafted sample (see Figure 1H). The sample showed stable capillary properties (tests 1–6 in Figure 1H).

The observed capillary action was promoted by the combined effects of the reduced contact angle within the grooves and their geometric features. In particular, the presence of oxides made

the grooves surface partially hydrophilic (namely,  $0^\circ < \theta_e < 90^\circ$ ) which, thanks to the V-shape of the grooves, promotes the formation of concave menisci. The synergistic combination of these two factors, according to the Laplace's equation, generates an under-pressure at the air–liquid interface responsible of the observed capillarity. Note that both effects described are essential to observe wicking: a droplet on a flat and partially hydrophilic surface would simply retain a spherical cap shape, while a V-shaped groove made of a hydrophobic material (namely,  $\theta_e \geq 90^\circ$ ) would not wick water. See Notes S1 and Note S2, Supporting Information for a complete analysis of the conditions required to observe wicking in an ideal V-shaped groove.

## 2.2. Durability and Surface Functionalization

The vertical wicking performance was extremely stable for several cycles of exposure to water (see Figure 1H). Thus, the

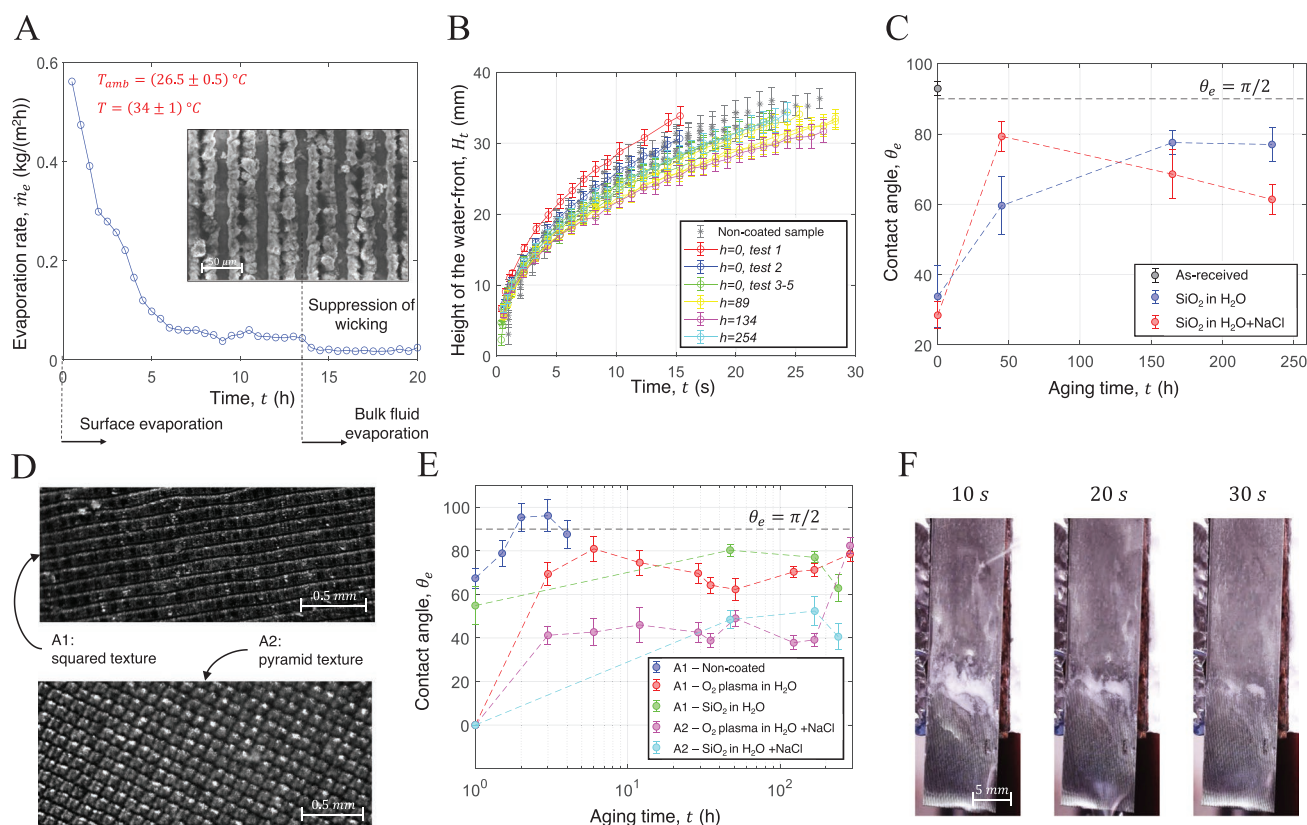


**Figure 2.** Durability of the proposed material. A) Durability test performed by evaporation and supplying the sample with  $\approx 1000 \text{ W m}^{-2}$ . The decrease in evaporation rate was due to progressive saturation of the active sites on the grooves surface, thus inhibiting hydrophilicity and capillarity. B) Long-term durability test of the grooved aluminum sample coated with SiO<sub>2</sub> by radio frequency sputtering. The capillary properties remained stable for more than 250 h of continuum immersion in distilled water (cyan data) and the performance was comparable with that of the as-machined sample (black data). Note that, without providing surface functionalization or coating, the as-processed grooved specimen lost its capillary properties after  $\approx 15$  h of exposure to water (see Video S2, Supporting Information). C) Contact angle measurements on flat aluminum plated coated with SiO<sub>2</sub> and aged in distilled water (blue data) and saltwater (red data). Both samples remained hydrophilic after  $\approx 250$  h of aging. D) Square (A1) and pyramid (A2) textures obtained on two aluminum sheets by fs-laser etching. The samples were used to investigate the effect of the texture on the durability of the obtained hydrophilicity and to compare the efficacy of the oxygen plasma treatment and SiO<sub>2</sub> coating. E) The as-machined A1 and A2 samples presented good hydrophilic properties, which however wore-out after a few immersion cycles (blue data). When functionalized with oxygen plasma (red and magenta data) or coated with SiO<sub>2</sub> (green and cyan data) the hydrophilicity remained stable and below  $90^\circ$  for more than 200 h of immersion both in distilled (sample A1) and saltwater (sample A2). F) Removal of salt crystals by gentle rinsing. Most crystals were removed within 40 s.

durability of the component was investigated by means of an evaporation test: the grooved aluminum sheet was used to wick water from a reservoir under controlled temperature and humidity conditions (see Note S3, Supporting Information). The measured evaporation rate  $\dot{m}_e$  was used to evaluate the stability of the wicking performance: consistent values of  $\dot{m}_e$  over time are related to a constant evaporating surface. The test results, performed with micro-filtered water, show a decreasing evaporation rate until, after 13 h, evaporation from the specimen had ceased (see Figure 2A). This result can be related to a change of surface chemistry rather than to a modification of topology. During the initial wicking transient, the grooves are permeated by the aqueous solution and tend to be drained by the evaporative rate. However, due to capillary force, water is constantly supplied from the underlying basin and the phenomenon continues as long as the capillary pressure remains unvaried. As the aqueous solution flows, the dissolved ions and contaminants tend to rapidly saturate the reactive sites of the

surface activated by the laser treatment, which are responsible for the observed hydrophilicity, thus inhibiting the capillary properties. To corroborate this hypothesis, SEM analysis of the sample used (see the inset of Figure 2A) revealed that crystal formations progressively covered the grooves surface without clogging the grooves completely (see Figure S3, Supporting Information). Furthermore, subsequent imbibition tests performed with the same sample revealed that the observed capillary properties were greatly reduced despite the fact that the grooves were not visibly clogged (see Video S2, Supporting Information). This evidence is in line with previous results reported in the literature of laser-treated aluminum.<sup>[23–26]</sup> Therefore, it is essential to increase the durability, for example, by using nanoscale coatings or surface functionalizations to ensure the long-term durability of the component in harsh and reactive operating conditions.

Consequently, two surface treatments were tested to improve the long-term durability of the sample, here intended as the

ability of the material to maintain its functional properties when facing normal operating conditions (that is, remaining hydrophilic when exposed to aqueous solutions): a coating by radio frequency (RF) sputtering of SiO<sub>2</sub> and a functionalization by oxygen plasma (see Experimental Section).

The RF sputtering technique was opted for its effectiveness in generating nanometer-thick layers of a wide range of materials, thus avoiding altering the original shape of the grooves, while SiO<sub>2</sub> was selected for its chemical stability, intrinsic hydrophilicity, and its ability to protect the substrate from reactive components possibly dissolved in the solution (i.e., Cl<sup>−</sup> ions<sup>[29]</sup>). On the other hand, plasma treatment is an inexpensive and widely used cleaning procedure, but is commonly known to lose effectiveness after a few cycles of use. Thus, immediately after being treated with oxygen plasma, the sample was exposed to water vapor to saturate its active sites with hydrophilic –OH groups. Both techniques (coating with SiO<sub>2</sub> and O<sub>2</sub> plasma) are easily scalable and applicable to large-scale production.<sup>[30,31]</sup>

First, the effect of the SiO<sub>2</sub> coating was tested on a grooved sample and on two untreated aluminum sheets. The former was aged in distilled water and its performance was tested by capillary rise experiments, while the flat sheets were aged in both distilled and saltwater (35 g L<sup>−1</sup>) and the effectiveness of the treatment was evaluated by contact angle measurements. The laser-etched sample maintained excellent capillary properties (see Figure 2B): the best performance was observed during the first test performed after being coated, which then slightly decreased until the third exposure (see red data in Figure 2B). All subsequent tests showed stable and comparable performance within their uncertainty, even after more than 250 h of continuous exposure to water (see Figure 2B, cyan data), corresponding to ≈1 month of continuous use for 8 h day<sup>−1</sup>. Note that the obtained capillary performance is comparable to that of the as-machined sample (see Figure 2B, black data), thus achieving long-term durability without compromising the capillary properties initially observed. Similarly, the two flat plates coated with SiO<sub>2</sub> exhibited excellent wetting properties after the treatment (see Figure 2C), reporting an average contact angle of  $\theta_c = (31 \pm 5)^\circ$ , which increased significantly after an initial exposure to the two solutions of ≈50 h. All the samples examined at the various aging stages exhibited values of contact angles lower than the as-received aluminum plates (see Figure 2C, black data), and well below the threshold value of 90°.

Subsequently, two different patterns, one with squares (A1) and one with pyramids (A2, see Figure 2D), were crafted to verify whether the observed hydrophilicity and its short duration was due to the high aspect ratio of the topology obtained by laser-machining and to compare the effectiveness of the oxygen plasma treatment to that of the SiO<sub>2</sub> coating. Obviously, since the two textures are different, the two samples are expected to exhibit different  $\theta_c$  regardless of the surface treatment applied. As anticipated, the combined effect of altered surface chemistry and texturing reduced the contact angles to  $\theta_c = (67 \pm 5)^\circ$  and  $\theta_c = (25 \pm 3)^\circ$  for A1 and A2, respectively (see Video S3, Supporting Information). However, as previously observed, the obtained hydrophilicity was depleted after a few immersion cycles in distilled water (see blue data in Figure 2E and Video S4, Supporting Information), making it unusable for the intended application. Then, SiO<sub>2</sub> coating and oxygen plasma

treatment were applied to both specimens and their performance was evaluated by contact angle measurements. While A1 was aged in distilled water, the effect of saltwater (35 g L<sup>−1</sup>) on the two functionalizations was investigated on A2. Both surface treatments strongly improved the hydrophilicity of the samples, which also showed capillary spreading after about 100 min of immersion in both solutions (see red, magenta, and cyan data in Figure 2E, and Video S5, Supporting Information for plasma-treated samples). Successively,  $\theta_c$  increased for all tested configurations but remained stably below 90° for more than 200 h of aging in both distilled and saltwater. The presented results proved that simple surface functionalizations or coatings can dramatically increase the stability of performance of the proposed concept, even when operating with salinity feeds.

The effect of precipitation or crystallization of contaminants on the sharp and rough surface of the grooves might lead to clogging and reduced performance. This condition might occur when operating with feeds at high salt concentrations and high evaporation rates and is one of the main challenges in applications like solar desalination.<sup>[32–35]</sup> Nevertheless, the salt crystals can be easily removed by gently rinsing the sample surface, even with salt or micro-filtered water, for ≈40 s (see Figure 2F and Video S6, Supporting Information).

### 2.3. Modeling and Experimental Evaluation of the Capillary Properties

Then, in order to compare the capillary properties obtained with those of other novel or commercial materials, both structured (i.e., with tailored and homogeneous pores) and unstructured (e.g., nonwoven fabrics), it is essential to relate the micro-structure of the proposed material to its capillary properties. In particular, the wicking performance can be described mainly in terms of capillary pressure  $p_c$  and absolute permeability  $K$ , which are functions of the surface chemistry (via  $\theta_c$ ) and geometry (via the height  $h_g$  and angle of inclination  $\alpha$ ) of the laser-etched grooves. Derivation of their analytical expression would allow the optimization of the groove design parameters for a target application and provide guidelines for the chosen machining technique, which may not be limited to femtosecond laser.

The crafted laser-etched pattern made the aluminum sheet a fully-fledged porous medium which, consequently, can be described using a suitable theoretical framework. However, the different geometry, surface roughness and state of oxidation related to each groove make it convenient to model the pattern as a simplified homogeneous array of smooth V-shaped cavities, each with the average geometric parameters assessed by SEM image analysis (see Figure 3A). Under this hypothesis, the classic approach to model analytically the time-dependent position of the water front  $H_t$  during wicking is the Lucas–Washburn model,<sup>[36,37]</sup> which predicts capillary rise by imposing the equilibrium between capillary and viscous forces, respectively  $F_c$  and  $F_\mu$ . However, this approach neglects the gravitational force  $F_g$ , which becomes predominant in vertical components designed to overcome small hydraulic heads and to deliver the fluid without relying on circulation pumps.<sup>[38,39]</sup> Thus, the 1D force balance was expressed as  $F_c = F_\mu + F_g$ . The capillary force

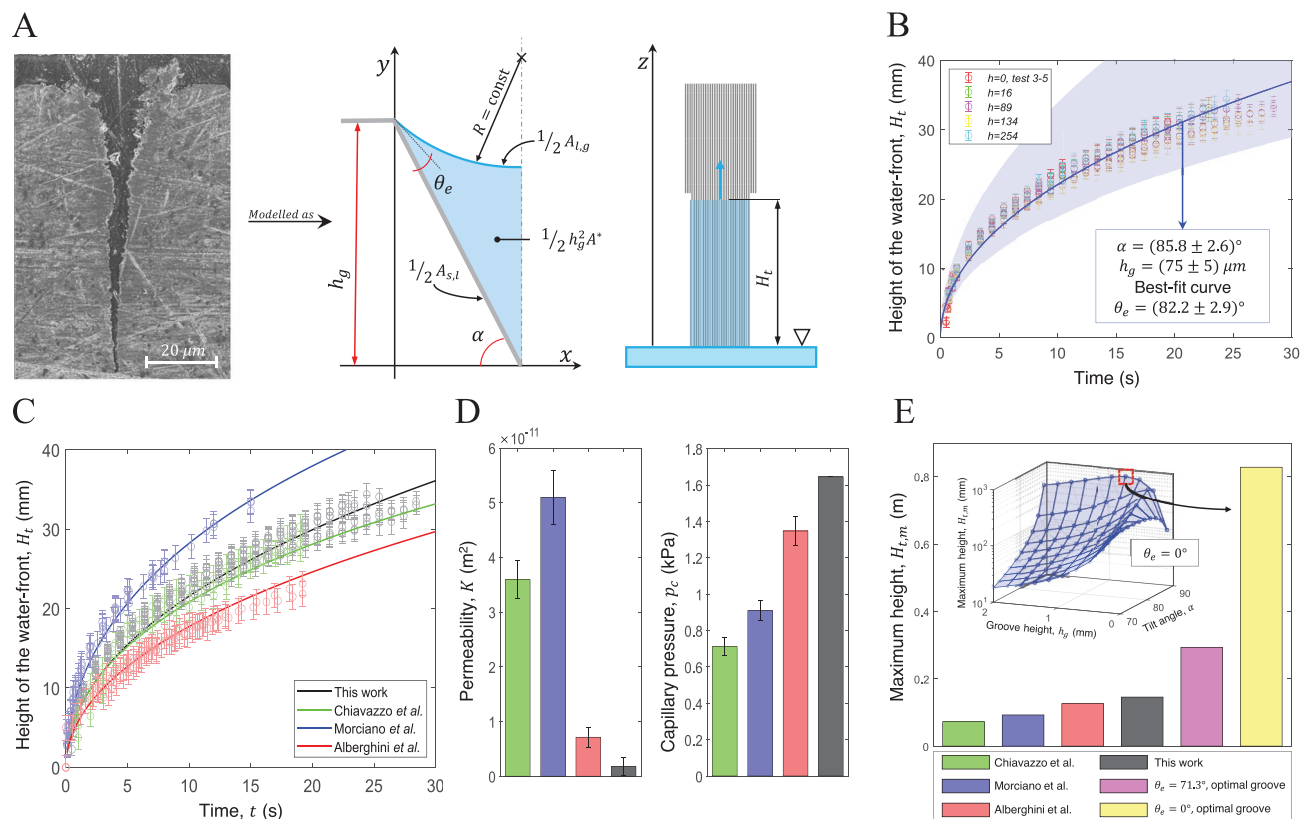


**Figure 3.** Experimental investigation and theoretical modeling of the obtained wicking performance. A) The crafted grooves were represented as an ideal array of identical and smooth V-shaped cavities and their capillary properties were modeled as a function of their height  $h_g$ , tilt angle  $\alpha$ , and contact angle  $\theta_e$ . The dynamic position of the water front  $H_t$  was modeled under the sharp-front approximation. B) The obtained data were used to fit the value of  $\theta_e$  from the theoretical model by the least-squares method. C,D) The wicking performance, capillary pressure  $p_c$ , and absolute permeability  $K$  of the crafted material (black data) were compared with those of other hydrophilic textiles used in passive applications (green, blue, and red data).<sup>[4,13,18]</sup> E) A novel dynamic model including the effect of evaporation in the wicking transient was used to predict and compare the performance of the proposed material (black bar), the reference textiles (green blue and red bars), and ideal V-shaped grooves with different hydrophilicity (pink and yellow bars). The theoretical predictions were performed considering a constant evaporation rate  $\dot{m}_e = 0.25 \text{ kg m}^{-2} \text{ h}^{-1}$  on the sample surface exposed to the environment.

$F_c$  was derived from the surface free energy per unit length, which is a function of the solid–liquid and liquid–gas contact areas,  $A_{s,l}$  and  $A_{l,g}$  respectively (see Figure 3A). Similarly, a water column of height  $z$  supported only by capillary forces is subject to a gravitational force  $F_g$  proportional to the groove cross section, that is,  $h_g^2 A^*$  (see Figure 3A), while the viscous force  $F_\mu$  was expressed by considering a Poiseuille flow (see Experimental Section). Under these assumptions, the force balance was used to derive an explicit analytical equation describing the position of the water front  $H_t$  in the  $z$ -direction for a given time  $t$  (see Experimental Section).

The model described allows to evaluate the wicking performance of the rigid capillary material by relying on three parameters only, which are related to the average geometry of the grooves (i.e., their height  $h_g$  and tilt angle  $\alpha$ ) and their surface chemistry (through the equilibrium contact angle  $\theta_e$ ). However, the oxidation of the cavities surface and their irregular roughness changed the value of  $\theta_e$  with respect to the one measured on the untreated aluminum surface. Thus, the apparent contact angle  $\theta_e$  was evaluated by least squares fitting of the theoretical position of the water front  $H_t$  on the experimental

data obtained, resulting in  $\theta_e = (82 \pm 3)^\circ$ . Note that the model fitting was performed on the data obtained from the aged sample coated by  $\text{SiO}_2$  (green, yellow, magenta, and cyan data in Figure 2B). The reported uncertainty on  $\theta_e$  was estimated through the fitting procedure by considering the experimental uncertainties of  $h_g$  and  $\alpha$ , which led to the shaded blue area in Figure 3B.

To assess the applicability of the proposed material, the capillary properties of the aged sample (see Figure 3C, black data) were compared with those of three other materials used for passive applications by means of vertical wicking tests: a polyethylene-based woven textile engineered for evaporative cooling<sup>[4]</sup> (see Figure 3C, red data) and two nonwoven fabrics employed in passive solar desalination devices<sup>[13,18]</sup> (see Figure 3C, green and blue data). The silica-coated aged material presents the second-best capillary performance with respect to the reference materials tested. The micro-porous structure of these materials is extremely different from that of the proposed material: the woven textile is composed of arrays of cylindrical fibers and its capillary properties can be ascribed to the size and arrangement of the fibers, while the nonwoven textiles can be considered as

a network of connected pores whose sizes can be expressed in terms of a probability distribution. The transport of a single-phase fluid in such different geometries can be modeled by the Darcy's law, where the porous matrix is described in terms of its volume-averaged properties: the capillary pressure  $p_c$ , absolute permeability  $K$  and effective porosity  $\phi$ . The Darcy's law and the continuity equation were combined and solved under the sharp-front approximation to derive another analytical expression of  $H_t$  (see Note S4, Supporting Information), which was then compared with the one derived for an ideal V-shaped groove, obtaining  $p_c = \gamma P^* (h_g A)^{-1}$ ,  $\phi = h_g (\delta \tan(\alpha))^{-1}$  and  $K = \phi h_g^2 A^* (8\pi)^{-1}$ . The wicking performance is enhanced by the increase of the capillary pressure and the absolute permeability. However, the geometrical parameters of the grooves have competing effects on  $p_c$  and  $K$ : the capillary pressure is promoted by sharp and short grooves, while the opposite holds for the absolute permeability, as wide and tall grooves reduce the viscous losses (see Figure S4, Supporting Information). Note that the contact angle  $\theta_c$  does not have an important effect on  $K$ , as it only affects the shape of the water meniscus modifying  $A_{i,g}$  (see Figure 3A), while it changes the values of  $p_c$  by different orders of magnitude. Thus, lower values of  $\theta_c$  are expected to have a major effect on the wicking performance. As the effective porosity and the capillary pressure of the reference textiles were evaluated experimentally (see Note S5, Supporting Information), the model was used to fit their absolute permeability from the vertical wicking data. The values of  $p_c$  and  $K$  obtained for the different materials are compared in Figure 3D. As it can be observed, while the suction pressure due to the grooves geometry exceeds the others, the permeability of the two ordered geometries (namely, the woven textile and the V-shaped grooves, red and black bars respectively) is approximately one order of magnitude lower. Therefore, being able to define an optimal geometry of the porous structure (i.e., the grooves) while maximizing the resulting capillary properties is crucial to increase their range of applicability and perform a correct design of the passive devices where they are put into use.

Most applications concerning capillary media in passive devices require evaporating the wicked liquid as it flows through the porous matrix. Consequently, evaporation affects the imbibition transient and, along with gravity, determines the maximum height reached by the water front  $H_{t,m}$ . This has a direct effect on the maximum size attainable for components relying on wicking and evaporation. Hence, the wicking model must include an average evaporation rate to correctly model the performances of the component. Therefore, a novel numerical scheme extending the classic approach based on the Darcy's law was implemented and validated against previous analytical solutions,<sup>[40]</sup> obtaining excellent agreement (see Note S6, Supporting Information). The model ascribes to the specific evaporation rate  $\dot{m}_e$ , which is considered constant over the sample surface, an extra pressure drop to the water flowing in the grooves. The explicit time discretization scheme used is particularly suited to investigate configurations at the dry-out limit, making it adequate to explore the limits of passive components for water transport. The model was used to evaluate  $H_{t,m}$  for the reference textiles (green, blue, and red bars in Figure 3E) when subject to evaporation in laboratory conditions. The

results were compared with the theoretical predictions for the proposed material (black bar in Figure 3E) and for other rigid supports with optimal V-shaped grooves with  $\theta_c = 71.3^\circ$ , typical of nylon<sup>[41]</sup> (pink bar), and  $\theta_c = 0^\circ$ , characteristic of a super-hydrophilic surface such as clean glass<sup>[42]</sup> (yellow bar). Note that different contact angles might be achieved by surface treatment, different types of coating or by choosing as rigid support a material which is inherently hydrophilic. The performance of the proposed material is comparable to the reference ones. However, when considering a lower contact angle, the performance of the laser-etched support exceeds that of traditional materials, which, due to their nonordered structure, have fewer degrees of freedom for further optimization. Note that the specific working condition should be considered in the optimization procedure (see the inset in Figure 3E for  $\theta_c = 0^\circ$ ): different evaporation rates affect the optimal value of  $h_g$  (see Figure S5, Supporting Information). The optimization algorithm favors extremely sharp angles, ideally up to  $89^\circ$ , which might entail processing and operability issues: while a large variety of applications rely on pure liquids (e.g., electronic cooling), others might be subject to crystallization or build-up of contaminants dispersed in the working fluid (e.g., water treatment and desalination). Therefore, the design and optimization of the grooves geometry should include not only the fluid transport, but also the constraints due to specific applications, the device working conditions and the chemical–physical interactions at the solid–liquid interface.

## 2.4. Discussion

An emerging and interesting engineering application of porous materials is represented by passive solar or thermal desalination, a viable and large-scale option to address water shortage. Several works proposed different novel materials allowing passive operations such as graphene-based materials,<sup>[43–46]</sup> carbonized bio-materials,<sup>[47,48]</sup> carbon-based materials,<sup>[49–53]</sup> polymers or hydrogels,<sup>[54,55]</sup> nanofluids and/or nanoparticles,<sup>[56–60]</sup> and metal oxides.<sup>[61]</sup> However, most of the designs proposed often include a single-stage evaporator and are constrained by the thermodynamic theoretical limit of  $1.5 \text{ L m}^{-2} \text{ h}^{-1}$ , which is far below the output of active systems. Multistage passive devices offer a solution to the issue: their design allows to recover the enthalpy of condensation of one stage to drive the evaporation in the next one, thus triggering a cascade process able to go beyond the single-stage limit. Recently, various multistage prototypes utilizing solar energy and nonstructured capillary materials were proposed and experimentally characterized.<sup>[13,18,27,28,62–64]</sup> Here we investigate the feasibility of replacing the traditional porous layer by embedding the developed laser-etched component in the device layout proposed by some of the authors<sup>[13,18]</sup> and successfully used as a reference in several following works.<sup>[19,63–65]</sup> This substitution allows to improve the compactness of multistage devices, thus increasing the number of stackable stages, and to simplify their assembly on an industrial scale. At the same time, it allows to increase the stability and repeatability of their performance and general quality. A schematic of the device is reported in Figure 4A and its layout and working principle can be briefly

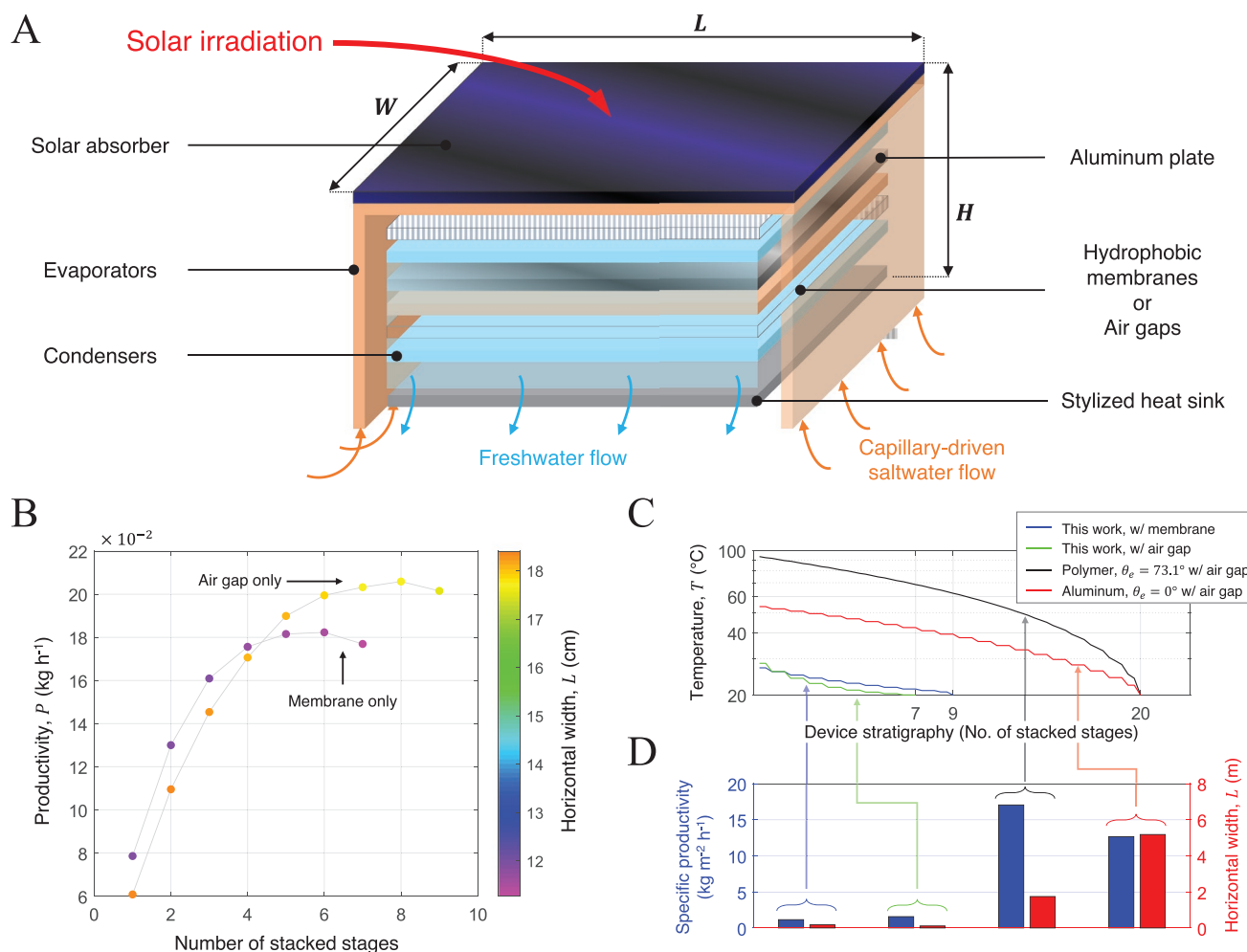


**Figure 4.** Passive solar desalination as a perspective application. A) Stratigraphy of the proposed passive device for solar desalination. The modular design allows to stack several stages to improve the overall productivity. For the sake of simplicity, only two stages were represented. B) Modeling predictions of the device productivity  $P$ , expressed in kg h<sup>-1</sup>, achievable by employing the proposed grooved aluminum layer in both evaporators and condensers, using either a hydrophobic membrane or an air gap. By varying the number of stacked stages, it is possible to identify the optimal configuration to maximize the device performance. The color bar reports the maximum horizontal width achievable  $L$ , highlighting how alternative layouts imply different operating evaporating surfaces. C) Temperature distribution through the representation of the device by thermal network, where the number of simulated stages was highlighted on the horizontal axis. The simulations were performed considering different properties of the substrates constituting the evaporators and condensers: a conductive aluminum sheet (blue, green, and red curves); a thermally insulating polymer (black curve); different levels of hydrophilicity (blue and green curves  $\theta_e = 84^\circ$ , black curve  $\theta_e = 73.1^\circ$ , red curve  $\theta_e = 0^\circ$ ). D) Specific productivity (blue bars) and maximum achievable horizontal width (red bars) of the configurations tested in panel C. The configuration reporting the highest specific productivity, may not present the highest overall productivity  $P$  due to poor capillary performance.

summarized as follows. The considered device shows a multistage configuration to recover the latent heat of condensation, thus enhancing the water productivity. Without losing generality, the schematic reported in Figure 4A is referred to a two-stages configuration device. Each stage is composed by an evaporator, an hydrophobic membrane or an air gap, and a condenser (see Figure 4A). The latter is placed in thermal contact with the evaporator of the subsequent stage by means of an aluminum plate, enabling latent heat recovery. Evaporators supply seawater to the device, while condensers collect and channel the freshwater out of the device into an external basin. As already anticipated, evaporators, and condensers are usually made of capillary porous media, thus being able to overcome small hydraulic heads (indicated with  $H$  in Figure 4A) and

deliver the working fluids throughout the system without the need of mechanical or electrical active components. The hydrophobic membrane avoids contamination between the evaporator and the condenser, as it cannot be crossed by water unless a given pressure is applied, which usually is orders of magnitude higher than the normal working pressure and depends on the membrane surface chemistry and average pores size. The first-stage evaporator is heated by an external heat source, usually solar irradiation, which is harvested by means of a selective highly-efficient absorber, while the last-stage condenser is in thermal contact with a larger heat reservoir—usually the saltwater reservoir itself—by means of a heat sink. In this way, a temperature gradient is imposed across the device and, thus, across the membranes of each stage. The counter-posing

interplay of the temperature and salinity gradients across the hydrophobic membrane imposes a net vapor pressure difference, thus generating a net vapor flux from the evaporator toward the condenser.<sup>[13,18]</sup> The condensation of water vapor leads to the release of enthalpy, therefore heating by conduction the evaporator of the adjacent stage driving further evaporation of saltwater.

A theoretical lumped-parameter model was developed to predict the achievable performance and size of the described desalination device, considering various materials, layouts, and operating conditions (see Experimental Section). First, the coupled model was used to evaluate the optimal configuration and overall productivity  $P$  of the desalination device when the proposed grooved material is employed in both condensers and evaporators (see Figure 4B). The achievable values of the maximum horizontal width  $L$  were indicated using the color bar. Considering a traditional layout, which requires the use of a hydrophobic membrane, the maximum predicted performance was obtained by combining six stages with a horizontal width of about 12 cm. Note that fewer stacked stages allow for larger evaporating surfaces (see the color bar in Figure 4B), as capillarity should overcome smaller hydraulic heads. However, the proposed rigid porous structure allows to replace the hydrophobic membranes with simple and cost-effective air gaps,<sup>[18]</sup> ensuring the planarity of the stack and, therefore, avoiding contamination between the two feeds. Since hydrophobic membranes are responsible for most of the cost of passive thermal desalination devices,<sup>[17]</sup> this concept appears to be an effective solution to significantly improve economic viability of passive thermal desalination devices. Therefore, the modeling predictions were repeated by substituting the membrane with a 0.5 mm air gap, allowing the most expensive and fragile component of the device to be replaced with an inexpensive and robust plastic frame. This configuration resulted in an  $\approx 30\%$  wider device, more stackable stages, and  $\approx 10\%$  higher values of  $P$ . The increase in performance is caused by the counterintuitive reduction in specific evaporative flux due to the air gap. As it can be seen in Figure 4C, the air gap configuration (green curve) results in a lower temperature profile than the membrane layout (blue curve), and, consequently, in a lower specific productivity (see the respective blue bars in Figure 4D). However, the reduced evaporation rate enables higher values of  $L$  before dry-out occurs, resulting in higher productivity. This analysis highlights how  $P$  is nonlinearly determined by these competing effects, making the proposed model a necessary tool to predict the optimal device configuration.

As mentioned above, the achievable specific productivity is determined by the temperature distribution within the device, which varies according to the environmental conditions (e.g., ambient temperature and solar irradiance), the heat transfer and mass properties of the materials used in the device (e.g., membrane permeability, thermal resistance between the stages, heat losses), and the number of stacked stages. Since higher temperature profiles are related to increased specific productivity, minimizing the heat losses toward the water reservoirs is crucial to maximize the device performance. Accordingly, the model was used to evaluate the effect of the properties of the capillary substrate in two additional configurations: an insulating polymer (e.g., nylon,  $\theta_c = 73.1^\circ$ ) and an ideally wettable

aluminum layer (namely,  $\theta_c = 0^\circ$ ), both provided with optimal grooves (whose shape was evaluated via the presented capillary model). Clearly, for equal number of stacked stages, the lower thermal conductivity of the configuration comprising the polymeric substrate (see Figure 4C, black line) reports a higher temperature profile than the one with aluminum (see Figure 4C, red line), and also results in higher specific productivity (see the respective blue columns in Figure 4D). However,  $P$  is determined by both the specific productivity (see blue bars in Figure 4D) and the maximum achievable horizontal width  $L$  (see blue bars in Figure 4D). Thus, the mediocre capillary performance of the polymer substrate limits  $L$  (see red bars in Figure 4D), and thus also the achievable  $P$  (see Figure S6, Supporting Information), emphasizing the reduced impact of thermal losses if better capillary properties provide a larger evaporating surface.

To enhance the device performance, the horizontal section of the evaporators must present high thermal conductivity to minimize the thermal losses within the stack. Simultaneously, it is also necessary to reduce conductive losses toward the reservoir, which, as analyzed above, would hinder the device productivity. Consequently, the vertical section of the evaporators must have low thermal conductivity. Disengaging from the engineering problem, the grooved layers were envisaged as multi-materials consisting of a vertical section of glass (hydrophilic and a good thermal insulator) and a horizontal section of aluminum, both with the same capillary properties (see Experimental Section). It is worth noting that this assumption is introduced solely on a theoretical level to show the impact of an ideal and thermally-anisotropic capillary layer, able to maximize the device performance in this particular application. In this scenario, a laser-etched multi-material with similar capillary properties as those achieved in this work allows to feed a 20-stages configuration device guaranteeing a productivity equal to  $1.5 \text{ kg h}^{-1}$  and width  $L$  equal to 8 cm (see Figure 5A). The predictions were also extended to the other two configurations tested, namely the nylon substrate and the ideally wettable aluminum sheet, both engraved with optimized grooves and the latter envisaged as a multi-material (i.e., with its vertical section made of glass). In a 20-stages configuration, the polymer-based material resulted in a productivity  $P = 30.0 \text{ kg h}^{-1}$  and horizontal extension  $L = 1.7 \text{ m}$ ; similarly, a 20-stages configuration employing the ideal multi-material allowed to achieve  $P = 95.4 \text{ kg h}^{-1}$  and  $L = 5.1 \text{ m}$  (see Figure 5A). It is worth noting that the productivity obtained optimizing the grooves geometry on an ideally hydrophilic material is approximately two orders of magnitude higher than the case study reported. Therefore, maximizing the capillary properties of the porous materials employed is crucial to maximize the overall performance of the device.

Finally, for the sake of completeness, a comparison between the performance of state-of-the-art devices and that of the proposed multistage device operating with the envisaged laser-etched multi-material component with the same capillary properties achieved in this work, evaluated via model extrapolation, is reported in Figure 5B. In detail, light blue and blue bars are referred to multistage and single-stage devices, respectively, able to perform a complete distillation cycle (namely, including both the evaporation and condensation processes). Instead, red bars are referred to devices able to perform a partial distillation

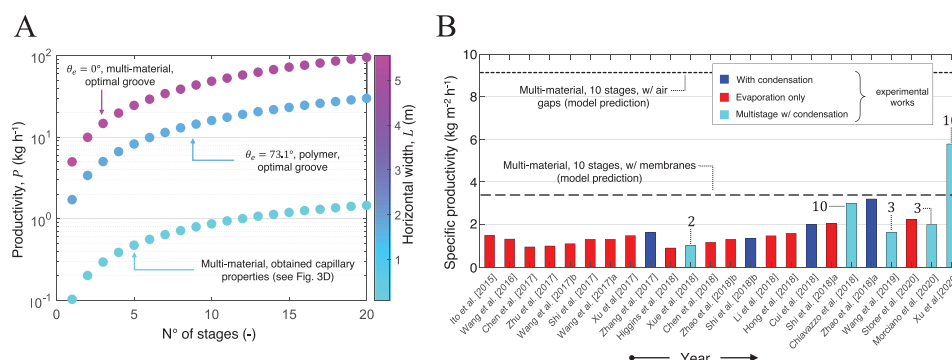


**Figure 5.** Performance extrapolation employing perspective multi-material substrates. A) Modeling predictions of productivity, maximum horizontal width  $L$ , and optimal number of stages for the passive desalination device. The dynamic capillary rise model and a lumped-parameters thermal model were coupled and used to evaluate the maximum length  $L$  achievable with a wicking material of known capillary properties, while avoiding dry-out. The predictions are referred to the air gap configuration. B) Comparison between the experimental performance of different passive solar desalination devices reported in the literature (colored bars) with those predicted by the proposed model (black dashed line), including or excluding the contribution of commercial hydrophobic membranes. The values reported above the multistage references refer to the number of modular stages tested.

cycle, where only evaporation takes place. The black dashed lines report the produced modeling predictions, which, for a fair comparison, were limited to 10-stage configurations. Interestingly, the use of the air gap alone allows the device to achieve a 165% increase in specific productivity with respect to the hydrophobic membrane configuration, and a 58% increase over the higher performing device<sup>[64]</sup> (see Figure 5B). Note that all the state-of-the-art devices considered were manufactured on a laboratory scale, with a maximum size of the order of centimeters, whereas the device envisaged here might be easily scaled to the order of meters. This highlights how disregarding the capillary properties of the materials selected when designing a passive device involving wicking and evaporation might significantly limit its performance and the scalability of the proposed technology. Furthermore, the rigid structure of the grooves allows easier and more precise assembly of the multistage device, compared to soft materials such as fabrics or hydrogels.

### 3. Conclusions

This work presents rigid and micro-structured capillary materials for passive energy-conversion devices based on water absorption and evaporation. A comprehensive theoretical framework of the mass transfer in open capillaries was developed and used to propose general design guidelines for components operating close to their dry-out limit.

V-shaped grooves were engraved on rigid aluminum sheets by femtosecond laser processing. As process-activated surfaces progressively lose their acquired hydrophilicity during operation due to the change of their surface chemistry, our samples were coated by  $\text{SiO}_2$  or functionalized with oxygen plasma. The samples were aged by continuous exposure to distilled or saltwater and presented stable hydrophilicity and capillary properties for the whole duration of the test (more than 250 h). Then, we demonstrated that salt clogging could be easily removed with a short and gentle rinse. Note that testing the durability and a worst-case application scenario of a novel material was essential to evaluate the critical aspects of the proposed

concept and derive guidelines for the development of novel, efficient and real-scale passive devices.

Finally, the obtained wicking performance of the silica-coated grooved sample was compared with that of three other materials used in well-established passive applications, showing the second best performance in short-term vertical imbibition tests. The experimental results were then interpreted by a novel time-discretized analytical model coupling the effect of the grooves geometry, hydrophilicity, and evaporation rate. The model was then used to predict the optimal values of the geometrical parameters of the grooves maximizing their transport properties. The results obtained from the characterization and the wicking tests proved the great potential of application and viability of the proposed concept.

The model was then coupled with a lumped-parameters heat and mass transfer model, envisioning the use of the proposed material in a passive multistage device for solar desalination. The combined models were essential to estimate the overall productivity of the assembly by predicting the maximum achievable length to avoid dry-out when operating under average mid-day conditions. The rigid capillary substrate allows the hydrophobic membranes to be replaced by air gaps: the proposed laser-etched aluminum could be used to assemble a eight-stages membrane-less device with a predicted specific productivity of  $1.6 \text{ kg h}^{-1} \text{ m}^{-2}$ . Then, envisaging the fabrication of a multi-material substrate with the same capillary properties obtained in this work, a 10-stages device could achieve a 58% higher specific productivity than the best-performing passive thermal device reported in the literature, for the same number of stages used and without relying on membranes. Note that the model extrapolations presented should be considered solely as a discussion of a relevant case study and guide the reader toward a more rational design of passive devices for energy conversion.

Concluding, the proposed modeling framework proved to be essential in the perspective of scale-up of passive components, as it relates the capillary properties of a specific material—whether structured or not—and the target working conditions to the maximum evaporating surface exploitable. Moreover, the perspective evaluation of different materials would allow the

exploration of processing techniques other than femtosecond laser etching, such as molding or forming, achieving high-quality geometric features while at the same time lowering costs and increasing the scalability of this novel class of materials. Thus, a combination of the adopted design approach and the structured rigid capillary materials paves the way for the transition from laboratory-scale prototypes, as those recently proposed in the field of desalination<sup>[28,64]</sup> and sustainable cooling,<sup>[17]</sup> to real-scale devices.

## 4. Experimental Section

**Crafting and Characterization of the Rigid Capillary Material:** Selective ablation treatment was carried out using a femtosecond laser with a wavelength of 515 nm and pulse length of 214 fs. The samples were attached to a bi-axial motorized air-bearing handling system by means of a special laboratory adhesive tape. The laser radiation exiting the femtosecond source was guided, by means of dielectric mirrors, toward a plane-convex focusing lens with a focal length of 150 mm. Thus, a Gaussian laser spot with a diameter of about 50  $\mu\text{m}$  was generated and kept in a fixed position. The linear grooves were generated by the unidirectional translation of the sample below the laser spot, which was focused at a depth of 100  $\mu\text{m}$  from the top surface of the sample. The movement speed of the linear axis was between 0.25 and 0.35  $\text{mm s}^{-1}$ . The laser was operated at a frequency of 3 kHz, with pulse energy equal to 100  $\mu\text{J}$ . The machining was performed with a constant flow of compressed air coaxial with the laser.

The preparations of the samples for the SEM imaging comprised a preliminary cleaning treatment by ultrasonic sonication in dichloromethane ( $\text{CH}_2\text{Cl}_2$ ) for 4 min and ultrasonication in methylbenzene for 4 min; the samples were rinsed with ethanol and dried for 15 min. The cleansing was followed by a 15 min oxygen-plasma treatment (100 W) and metallization with platinum by radio frequency sputtering. The cross-sectional images were obtained by cutting a 5 mm portion from the cleaned sample, which was mounted on a spring, cemented in epoxy resin and polished with abrasive paper (4000 grit). The cross-sectional images were obtained with a InLens detector with a 30  $\mu\text{m}$  opening at an accelerating voltage of 4, 5, and 7.5 kV, while the surface morphology was observed applying a 50° tilt angle and an accelerating voltage of 8.5 kV. The EDS analysis was performed on uncleaned samples directly after the engraving process.

**Measurement of the Aluminum–Water Contact Angle on the Aluminum Sheets:** The contact angle between distilled water and a pristine aluminum sheet (Goodfellow, 5 cm  $\times$  5 cm sheets, 200  $\mu\text{m}$  thick, purity >99%) was measured by the sessile drop method. Both surfaces of the pristine aluminum sheet were tested after being cleaned with isopropyl alcohol, dried, and then washed with de-ionized water and dried in open air. The drops were placed on the sample surface with a micro syringe and photographed by an optical microscope (RS PRO, 5M pixel of resolution). A ruler (RS PRO, 0.5 mm of resolution) was used to calibrate the images. The contact angle was evaluated by measuring the height  $h_d$  and half-width  $L_d$  of the droplets (see Figure S7, Supporting Information), under the assumption of negligible effect of gravity, namely  $L_d \ll \sqrt{\gamma/(\rho g)}$ ,<sup>[66]</sup> which was experimentally verified for each droplet. See Note S7, Supporting Information for further details.

**Vertical Wicking Tests:** The experimental setup used to perform the vertical wicking measurements (see Figure S8, Supporting Information) included a 1 cm  $\times$  5 cm sample of the laser-etched aluminum sheet, a mechanical vertical stage, a metal bar fixed on an adjustable support, an optical microscope (RS PRO, 5M pixel of resolution), a ruler (RS PRO, 0.5 mm of resolution), and a basin filled with distilled water. The sample was suspended from the metal bar by a clip, while the water basin was placed on the adjustable vertical stage beneath the hanged sample. Before the beginning of the wicking test, the video resolution was calibrated by taking a snapshot of the metal ruler placed next to

the hanged sample. The vertical stage was moved to dip  $\approx 2$  mm of the sample, while the position of the advancing water front was recorded by the optical microscope. The images acquired were post-processed via a MATLAB script to measure the time-dependent position of the water front  $H_t$  (see Figure S8, Supporting Information). At the end of the test, the sample was removed from the clip and dried in open air for more than 3 h before the test was repeated.

**Surface Coating and Functionalization:** For the functionalization by oxygen plasma, first, the samples were sonicated in ethanol (3 min) and MilliQ water (3 min) and dried with  $\text{N}_2$  flux. Subsequently a plasma treatment was performed in a reactive ion etching system (RIE, SAMCO 10-NR) for 10 min at a pressure of 50 Pa, applying a power of 50 W and  $\text{O}_2$  flux of 50 standard cubic centimeters per minute. Finally, the obtained samples were stored in a vacuum bag after insulating nitrogen for about 1 min.

Similarly, for the  $\text{SiO}_2$  coating, the samples were sonicated in ethanol (3 min) and MilliQ water (3 min) and dried with  $\text{N}_2$  flux. Subsequently a plasma treatment was performed in a RIE system (SAMCO 10-NR) for 10 min at a pressure of 50 Pa, applying a power of 50 W and  $\text{O}_2$  flux of 50 sscm. Then, a conformal layer of  $\approx 50$  nm of silica was deposited by RF sputtering (Moorfield) at a pressure of 3 Pa and applying a power of 75 W for 3300 s.

**Theoretical Model of Water Transport in a V-Shaped Groove:** The capillary force  $F_c$  in micro-porous media was determined by the interplay of the physicochemical properties of the three phases present in the system: the solid porous matrix; a first fluid, generally gaseous (i.e., air); a second fluid, generally liquid (i.e., water). The balance of forces at the contact line between the three phases produced a curvature of the fluid–fluid interface, which generated a pressure difference across the interface itself according to the Laplace's equation:<sup>[66]</sup> the shape of the interface, thus its curvatures, determined which fluid wets the porous matrix, filling its pores. Neglecting the effect of gravity and considering the groove entirely filled by water in the y-direction (see proofs in Notes S1 and S2, Supporting Information), the Laplace's pressure can be expressed as a function of a single, constant radius of curvature  $R$  (see Figure 3A). Thus, the Laplace's equation was integrated to obtain  $R = h_g/[\tan(\alpha)\sin(\alpha - \theta_g)]$  (see Note S2, Supporting Information), which relates the meniscus shape, thus the capillary pressure, solely to the grooves geometry and surface chemistry. In this simplified approach, the capillary force  $F_c$  can be evaluated from the 1D space derivative of the free energy per unit length, namely  $F_c = -dE/dz$ . In particular, the free energy per unit length  $E$  can be evaluated considering the solid–liquid and liquid–gas contact areas per unit length,  $A_{s,l}$  and  $A_{l,g}$  respectively (see Figure 3A), which can be easily evaluated with the analytical expression for  $R$  derived above; thus,  $F_c = h_g\gamma P^*$ , where  $P^*$  is a function of  $\alpha$  and  $\theta_g$  (see Note S8, Supporting Information). The gravitational force was evaluated as  $F_g = \rho g z h_g^2 A^*$ , where  $\rho$  and  $g$  are the water density and gravitational acceleration respectively,  $h_g^2 A^*$  is the cross section of the groove occupied by water (see Figure 3A) and  $A^*$  is a function of  $\alpha$  and  $\theta_g$ . The viscous force  $F_\mu$  was expressed considering a Poiseuille flow, assuming that the viscous losses are determined by the cross section  $h_g^2 A^*$  rather than by the meniscus shape (see Note S8, Supporting Information). Thus, the 1D force balance can be rewritten as a nonlinear first order differential equation, which can be solved to obtain an analytical expression for the water front position:  $H_t = B^{-1}[1 + W_0(-\exp(-1 - B^2 t(8\pi\mu A)^{-1}))]$ , where  $A = h_g P^*/\gamma$ ,  $B = h_g^2 A^* \rho g$  and  $W_0$  is the main branch of the Lambert function (see Note S8, Supporting Information for a detailed proof).

**Performance Predictions of the Desalination Device:** The Maxwell–Stefan and Dusty–Gas models were implemented to consider the molecule–molecule and molecule–matrix interactions (see Note S9, Supporting Information) and coupled with the time-discretized wicking model described (see Note S6, Supporting Information). The resulting comprehensive theoretical framework allowed estimating the maximum size achievable by the desalination device while avoiding dry-out, while simultaneously accounting for incident solar irradiation, ambient temperature, and number of phases. The performance predictions were obtained considering seawater with NaCl concentration equal to 35 g  $\text{L}^{-1}$  and incident solar irradiation of 1000  $\text{W m}^{-2}$ . The considered selective solar absorber had a solar absorbance equal to 0.95 and a limited

infrared emissivity equal to 0.04. A transparent insulator reducing the natural convection (three layers, each consisting of an ABS frame used to maintain two films of polypropylene 2 mm apart) was considered as placed on top of the selective absorber and was included in the model with an heat transfer coefficient of  $5 \text{ W m}^{-2} \text{ K}^{-1}$ . On the other hand, the aluminum heat sink placed at the bottom of the full stack led to an enhanced heat transfer coefficient equal to  $150 \text{ W m}^{-2} \text{ K}^{-1}$ , improving the heat dissipation and thus the temperature gradient across the device. Salt and distilled water were considered as separated by hydrophobic membranes (150  $\mu\text{m}$  thick, porosity of 0.8, and average pore size of 1  $\mu\text{m}$ ) or by air gaps 0.5 mm thick and with unitary porosity. The total size of the device, and thus the related evaporating area, is equal to  $W \times L$  (see the schematics reported in Figure 4A), where  $W$  was kept constant for all the considered case studies and equal to 1 m, whilst  $L$  was the design parameter evaluated by the coupled model. Note that  $W$  does not affect the modeling predictions. Then, based on the thermal properties of the materials, the micro-structure of the porous layers, and the solar irradiation, the model estimated the maximum horizontal size (namely,  $L_{\text{hz},m}$ ) that the multistage device could not exceed in order to avoid dry-out phenomena. Note that the conservative criterion  $L \leq 0.9 \times L_{\text{hz},m}$  was applied. The modeling predictions shown in Figure 4 were performed considering several configurations of the capillary substrates constituting the evaporators and condensers: the proposed laser-etched material, namely a grooved aluminum sheet with the same capillary properties shown in Figure 3D; a polymer substrate with  $\theta_c = 73.1^\circ$  and optimized grooves (resulting in  $K = 8.23 \times 10^{-11} \text{ m}^2$  and  $p_c = 4.26 \text{ kPa}$ ); an ideally wettable aluminum sheet with  $\theta_c = 0^\circ$  and optimized grooves (resulting in  $K = 1.59 \times 10^{-10} \text{ m}^2$  and  $p_c = 12.16 \text{ kPa}$ ). The multi-material envisaged were supposed to be composed by glass (with thermal conductivity  $0.8 \text{ W m}^{-1} \text{ K}^{-1}$ ) and aluminum (with thermal conductivity  $290 \text{ W m}^{-1} \text{ K}^{-1}$ ) on the vertical and horizontal sections, respectively. The materials were assumed to have homogeneous capillary properties, equal to those of the two aluminum substrates (namely, the one tested and the ideally wettable one) reported above, and were used to obtain the modeling predictions shown in Figure 5. Therefore, the thermal conductivity of the saturated vertical section was determined by averaging the thermophysical properties of water and glass, while that of the horizontal section was evaluated as the average of the thermophysical properties of water and aluminum. Both averages were weighted by the porosity of the considered substrate  $\phi$ .

**Statistical Analysis:** The combined uncertainties of experimental measurements were estimated as:<sup>[67]</sup>  $U = k\sqrt{u_A^2 + u_B^2}$ , where  $u_A$  are the uncertainty components estimated from the statistical analysis of the measured values,  $u_B$  are the uncertainty components estimated from a priori information (i.e., calibration, resolution, and accuracy of each measuring instrument employed),  $k = 2$  is the coverage factor. If the sample size was larger than 30 measurements, the uncertainty components  $u_A$  were estimated as the standard deviation of the data set; otherwise, they were estimated as  $u_A = 0.5|x_{\text{max}} - x_{\text{min}}|$ . All the error bars reported in the figures show a  $\pm U$  interval.

## Supporting Information

Supporting Information is available from the Wiley Online Library or from the author.

## Acknowledgements

The authors acknowledge the Clean Water Center @PoliTo and the partial financial support of the Italian National Project PRIN Heat Transfer and Thermal Energy Storage Enhancement by Foams and Nanoparticles (2017F7KZWS). The authors thank Dario Pezzini for supporting the experimental characterization.

Open Access Funding provided by Politecnico di Torino within the CRUI-CARE Agreement.

## Conflict of Interest

The authors declare no conflict of interest.

## Data Availability Statement

The data that support the findings of this study are available from the corresponding author upon reasonable request.

## Keywords

capillary materials, passive devices, textured materials, water-energy nexus

Received: February 9, 2022  
Revised: March 23, 2022  
Published online: May 23, 2022

- [1] N. A. Dudukovic, E. J. Fong, H. B. Gerneda, J. R. DeOtte, M. R. Cerón, B. D. Moran, J. T. Davis, S. E. Baker, E. B. Duoss, *Nature* **2021**, 595, 58.
- [2] P. Liu, G.-F. Chen, *Porous Materials: Processing and Applications*, Elsevier, New York **2014**.
- [3] B. Buonomo, A. di Pasqua, O. Manca, S. Nardini, *Appl. Therm. Eng.* **2020**, 176, 115456.
- [4] M. Alberghini, S. Hong, L. M. Lozano, V. Korolovych, Y. Huang, F. Signorato, S. H. Zandavi, C. Fucetola, I. Uluturk, M. Y. Tolstorukov, G. Chen, P. Asinari, R. M. Osgood III, M. Fasano, S. V. Boriskina, *Nat. Sustainability* **2021**, 4, 715.
- [5] J. Lee, J. Kim, T. Hyeon, *Adv. Mater.* **2006**, 18, 2073.
- [6] S. C. Singh, M. ElKabbash, Z. Li, X. Li, B. Regmi, M. Madsen, S. A. Jalil, Z. Zhan, J. Zhang, C. Guo, *Nat. Sustainability* **2020**, 3, 938.
- [7] S. J. Hollister, *Nat. Mater.* **2005**, 4, 518.
- [8] M. E. Davis, *Nature* **2002**, 417, 813.
- [9] M. Fasano, L. Ventola, F. Calignano, D. Manfredi, E. P. Ambrosio, E. Chiavazzo, P. Asinari, *Int. Commun. Heat Mass Transfer* **2016**, 74, 36.
- [10] L. Ventola, M. Fasano, R. Cappabianca, L. Bergamasco, F. Clerici, L. Scaltrito, E. Chiavazzo, P. Asinari, *Energies* **2020**, 13, 1360.
- [11] S. V. Boriskina, A. Raza, T. Zhang, P. Wang, L. Zhou, J. Zhu, *MRS Bull.* **2019**, 44, 59.
- [12] M. Morciano, M. Fasano, U. Salomov, L. Ventola, E. Chiavazzo, P. Asinari, *Sci. Rep.* **2017**, 7, 11970.
- [13] E. Chiavazzo, M. Morciano, F. Viglino, M. Fasano, P. Asinari, *Nat. Sustainability* **2018**, 1, 763.
- [14] S.-L. Wu, H. Chen, H.-L. Wang, X. Chen, H.-C. Yang, S. B. Darling, *Environ. Sci.: Water Res. Technol.* **2021**, 7, 24.
- [15] C. Zhang, Y. Shi, L. Shi, H. Li, R. Li, S. Hong, S. Zhuo, T. Zhang, P. Wang, *Nat. Commun.* **2021**, 12, 998.
- [16] L. Zhao, B. Bhatia, L. Zhang, E. Strobach, A. Leroy, M. K. Yadav, S. Yang, T. A. Cooper, L. A. Weinstein, A. Modi, S. B. Kedare, G. Chen, E. N. Wang, *Joule* **2020**, 4, 2733.
- [17] M. Alberghini, M. Morciano, M. Fasano, F. Bertiglia, V. Fernicola, P. Asinari, E. Chiavazzo, *Sci. Adv.* **2020**, 6, eaax5015.
- [18] M. Morciano, M. Fasano, S. V. Boriskina, E. Chiavazzo, P. Asinari, *Energy Environ. Sci.* **2020**, 13, 3646.
- [19] C. Chen, Y. Kuang, L. Hu, *Joule* **2019**, 3, 683.
- [20] S. H. Kim, G. C. Lee, J. Y. Kang, K. Moriyama, M. H. Kim, H. S. Park, *Int. J. Heat Mass Transfer* **2015**, 91, 1140.

- [21] A. Olanrewaju, M. Beaugrand, M. Yafia, D. Juncker, *Lab Chip* **2018**, 18, 2323.
- [22] L. Ventola, L. Scaltrito, S. Ferrero, G. Maccioni, E. Chiavazzo, P. Asinari, *J. Phys.: Conf. Ser.* **2014**, 525, 012017.
- [23] J. Drellich, E. Chibowski, D. D. Meng, K. Terpilowski, *Soft Matter* **2011**, 7, 9804.
- [24] S. Divin-Mariotti, P. Amieux, A. Pascale-Hamri, V. Auger, G. Kermouche, F. Valiorgue, S. Valette, *Appl. Surf. Sci.* **2019**, 479, 344.
- [25] A.-M. Kietzig, M. Negar Mirvakili, S. Kamal, P. Englezos, S. G. Hatzikiriakos, *J. Adhes. Sci. Technol.* **2011**, 25, 2789.
- [26] P. Bizi-Bandoki, S. Valette, E. Audouard, S. Benayoun, *Appl. Surf. Sci.* **2013**, 273, 399.
- [27] G. Antonetto, M. Morciano, M. Alberghini, G. Malgaroli, A. Ciocia, L. Bergamasco, F. Spertino, M. Fasano, *J. Cleaner Prod.* **2021**, 318, 128464.
- [28] M. Morciano, M. Fasano, L. Bergamasco, A. Albiero, M. L. Curzio, P. Asinari, E. Chiavazzo, *Appl. Energy* **2020**, 258, 114086.
- [29] D. Vasconcelos, J. Carvalho, M. Mantel, W. Vasconcelos, *J. Non-Cryst. Solids* **2000**, 273, 135.
- [30] K.-H. Choi, J.-A. Jeong, J.-W. Kang, D.-G. Kim, J. K. Kim, S.-I. Na, D.-Y. Kim, S.-S. Kim, H.-K. Kim, *Sol. Energy Mater. Sol. Cells* **2009**, 93, 1248.
- [31] L. Bonandini, N. Barbero, K. Costabello, C. Pavan, F. Parisi, G. Viscardi, *ChemSusChem* **2010**, 3, 591.
- [32] P. Tao, G. Ni, C. Song, W. Shang, J. Wu, J. Zhu, G. Chen, T. Deng, *Nat. Energy* **2018**, 3, 1031.
- [33] Z. Wang, T. Horseman, A. P. Straub, N. Y. Yip, D. Li, M. Elimelech, S. Lin, *Sci. Adv.* **2019**, 5, eaax0763.
- [34] L. Zhang, Z. Xu, L. Zhao, B. Bhatia, Y. Zhong, S. Gong, E. N. Wang, *Energy Environ. Sci.* **2021**, 14, 1771.
- [35] Y. Zhang, T. Xiong, D. K. Nandakumar, S. C. Tan, *Adv. Sci.* **2020**, 7, 1903478.
- [36] R. Rye, J. Mann, F. Yost, *Langmuir* **1996**, 12, 555.
- [37] D. Yang, M. Krasowska, C. Priest, M. N. Popescu, J. Ralston, *J. Phys. Chem. C* **2011**, 115, 18761.
- [38] E. W. Washburn, *Phys. Rev.* **1921**, 17, 273.
- [39] R. Masoodi, K. M. Pillai, *Wicking in Porous Materials: Traditional and Modern Modeling Approaches*, CRC Press, Boca Raton, FL **2012**.
- [40] N. Fries, K. Odic, M. Conrath, M. Dreyer, *Journal Colloid Interface Sci.* **2008**, 321, 118.
- [41] T. Hata, Y. Kitazaki, T. Saito, *J. Adhes.* **1987**, 21, 177.
- [42] D. Quéré, *Rep. Prog. Phys.* **2005**, 68, 2495.
- [43] Y. Ito, Y. Tanabe, J. Han, T. Fujita, K. Tanigaki, M. Chen, *Adv. Mater.* **2015**, 27, 4302.
- [44] L. Shi, Y. Wang, L. Zhang, P. Wang, *J. Mater. Chem. A* **2017**, 5, 16212.
- [45] P. Zhang, J. Li, L. Lv, Y. Zhao, L. Qu, *ACS Nano* **2017**, 11, 5087.
- [46] L. Cui, P. Zhang, Y. Xiao, Y. Liang, H. Liang, Z. Cheng, L. Qu, *Adv. Mater.* **2018**, 30, 1706805.
- [47] N. Xu, X. Hu, W. Xu, X. Li, L. Zhou, S. Zhu, J. Zhu, *Adv. Mater.* **2017**, 29, 1606762.
- [48] M. Zhu, Y. Li, G. Chen, F. Jiang, Z. Yang, X. Luo, Y. Wang, S. D. Lacey, J. Dai, C. Wang, C. Jia, J. Wan, Y. Yao, A. Gong, B. Yang, Z. Yu, S. Das, L. Hu, *Adv. Mater.* **2017**, 29, 1704107.
- [49] M. Higgins, A. S. Rahman, R. R. Devarapalli, M. V. Shelke, N. Jha, *Sol. Energy* **2018**, 159, 800.
- [50] Y. Wang, L. Zhang, P. Wang, *ACS Sustainable Chem. Eng.* **2016**, 4, 1223.
- [51] C. Chen, Y. Li, J. Song, Z. Yang, Y. Kuang, E. Hitz, C. Jia, A. Gong, F. Jiang, J. Zhu, B. Yang, J. Xie, L. Hu, *Adv. Mater.* **2017**, 29, 1701756.
- [52] H. Ghasemi, G. Ni, A. M. Marconnet, J. Loomis, S. Yerci, N. Miljkovic, G. Chen, *Nat. Commun.* **2014**, 5, 4449.
- [53] X. Huang, Y.-H. Yu, O. L. de Llergo, S. M. Marquez, Z. Cheng, *RSC Adv.* **2017**, 7, 9495.
- [54] Q. Chen, Z. Pei, Y. Xu, Z. Li, Y. Yang, Y. Wei, Y. Ji, *Chem. Sci.* **2018**, 9, 623.
- [55] F. Zhao, X. Zhou, Y. Shi, X. Qian, M. Alexander, X. Zhao, S. Mendez, R. Yang, L. Qu, G. Yu, *Nat. Nanotechnol.* **2018**, 13, 489.
- [56] J. Wang, Y. Li, L. Deng, N. Wei, Y. Weng, S. Dong, D. Qi, J. Qiu, X. Chen, T. Wu, *Adv. Mater.* **2017**, 29, 1603730.
- [57] X. Wang, Y. He, X. Liu, L. Shi, J. Zhu, *Sol. Energy* **2017**, 157, 35.
- [58] J. Zhao, Y. Yang, C. Yang, Y. Tian, Y. Han, J. Liu, X. Yin, W. Que, *J. Mater. Chem. A* **2018**, 6, 16196.
- [59] S. Hong, Y. Shi, R. Li, C. Zhang, Y. Jin, P. Wang, *ACS Appl. Mater. Interfaces* **2018**, 10, 28517.
- [60] X. Li, J. Li, J. Lu, N. Xu, C. Chen, X. Min, B. Zhu, H. Li, L. Zhou, S. Zhu, T. Zhang, J. Zhu, *Joule* **2018**, 2, 1331.
- [61] Y. Shi, R. Li, Y. Jin, S. Zhuo, L. Shi, J. Chang, S. Hong, K.-C. Ng, P. Wang, *Joule* **2018**, 2, 1171.
- [62] G. Xue, Q. Chen, S. Lin, J. Duan, P. Yang, K. Liu, J. Li, J. Zhou, *Global Challenges* **2018**, 2, 1800001.
- [63] W. Wang, Y. Shi, C. Zhang, S. Hong, L. Shi, J. Chang, R. Li, Y. Jin, C. Ong, S. Zhuo, P. Wang, *Nat. Commun.* **2019**, 10, 3012.
- [64] Z. Xu, L. Zhang, L. Zhao, B. Li, B. Bhatia, C. Wang, K. L. Wilke, Y. Song, O. Labban, J. H. Lienhard, R. Wang, E. N. Wang, *Energy Environ. Sci.* **2020**, 13, 830.
- [65] W. Wang, Y. Shi, C. Zhang, R. Li, M. Wu, S. Zhuo, S. Aleid, P. Wang, *Nano Lett.* **2021**, 21, 5068.
- [66] P.-G. De Gennes, F. Brochard-Wyart, D. Quéré, *Capillarity and Wetting Phenomena: Drops, Bubbles, Pearls, Waves*, Springer Science, Cham **2013**.
- [67] BIPM, IEC, IFCC, ILAC, ISO, IUPAC, IUPA, OIML, Evaluation of Measurement Data – Guide to the Expression of Uncertainty in Measurement, Joint Committee for Guides in Metrology, College Station, TX **2008**.